Earth and Planetary Science Letters 560 (2021) 116795

Contents lists available at ScienceDirect

Earth and Planetary Science Letters

www.elsevier.com/locate/epsl

The 2010 Haiti earthquake revisited: An acoustic intensity map from remote atmospheric infrasound observations

Shahar Shani-Kadmiel [a,b,*], Gil Averbuch [a,b], Pieter Smets [a,b], Jelle Assink [b], Läslo Evers [b,a]

[a] Faculty of Civil Engineering and Geosciences, Department of Geoscience and Engineering, Delft University of Technology, Delft, the Netherlands
[b] R&D Seismology and Acoustics, Royal Netherlands Meteorological Institute (KNMI), De Bilt, the Netherlands

ARTICLE INFO

Article history:
Received 21 July 2020
Received in revised form 23 January 2021
Accepted 29 January 2021
Available online 10 February 2021
Editor: R. Bendick

Keywords:
ShakeMap
infrasound
seismo-acoustics
beamforming
numerical modeling

ABSTRACT

In the days following the January 12, 2010 M_w 7 Haiti earthquake the shaking intensity near the epicenter was overestimated and the spatial extent of the potentially damaging shaking was underestimated. This was due to the lack of seismometers in the near-source region at the time of the earthquake. Besides seismic waves, earthquakes generate infrasound, i.e., inaudible acoustic waves in the atmosphere. Here we show that infrasound signals, detected at distant ground-based stations, can be used to generate a map of the acoustic intensity, which is proportional to the shaking intensity. This is demonstrated with infrasound from the 2010 Haiti earthquake detected in Bermuda, over 1700 km away. Wavefront parameters are retrieved in a beamforming process and are backprojected to map the measured acoustic intensity to the source region. The backprojection process accounts for horizontal advection effects due to winds and inherent uncertainties with regard to the time of detection and the back azimuth resolution. Furthermore, we resolve the ground motion polarity in the epicentral region and use synthetics generated by an extended infrasound source model to support this result. Infrasound measurements are conducted globally for the verification of the Comprehensive Nuclear-Test-Ban Treaty and although the network was designed to provide global coverage for nuclear explosions in the atmosphere, it is shown in this paper that there is also global coverage for the estimation of acoustic shaking intensity. In this study, we lay the groundwork that can potentially make infrasound-based ShakeMaps a useful tool alongside conventional ShakeMaps and a valuable tool for earthquake disaster mitigation in sparsely monitored regions.

1. Introduction

The January 12, 2010 M_w 7 Haiti earthquake is one of the most devastating earthquake disaster in recent history. This earthquake was preceded by several historical earthquakes that have severely damaged the city of Port-au-Prince throughout history (Bilham, 2010). However, no research-quality seismic stations were operating in Haiti prior to this earthquake (Hough et al., 2010; Douilly et al., 2013).

To rapidly assess the potential impact and the necessary response measures following an earthquake, the U.S. Geological Survey (USGS) launched the Prompt Assessment of Global Earthquake for Response (PAGER) in 2007 (Jaiswal et al., 2011). A key component of the PAGER system is the *ShakeMap*, which indicates the earthquake impact through the distribution of shaking intensity. The severity of ground shaking generally decreases with distance from the epicenter, however, near-surface geology, topography, and the source radiation pattern, contribute to local variations in ground shaking intensity. Whereas earthquake source characteristics, e.g., location and magnitude, can be rapidly determined using distant seismic stations, rapid generation of an accurate ShakeMap requires ground motion measurements from stations in the near-source region (Earle et al., 2009). Due to the lack of seismometers during the 2010 Haiti earthquake disaster, the initial ShakeMaps overestimated the shaking intensity near the epicenter and underestimated the spatial extent of the potentially damaging shaking (Fig. 1).

Much scientific work has been carried out in Haiti following the 2010 earthquake disaster. These efforts included constructing the initial seismic hazard maps (Frankel et al., 2010), deploying seismic stations to record and precisely locate aftershocks, gaining insight into the faulting mechanisms and ground motion characteristics in the region (Hough et al., 2010; Mercier de Lépinay et al., 2011), estimating peak ground acceleration from rigid body displacement

* Corresponding author at: Faculty of Civil Engineering and Geosciences, Department of Geoscience and Engineering, Delft University of Technology, Delft, The Netherlands.
E-mail address: s.shanikadmiel@tudelft.nl (S. Shani-Kadmiel).

https://doi.org/10.1016/j.epsl.2021.116795

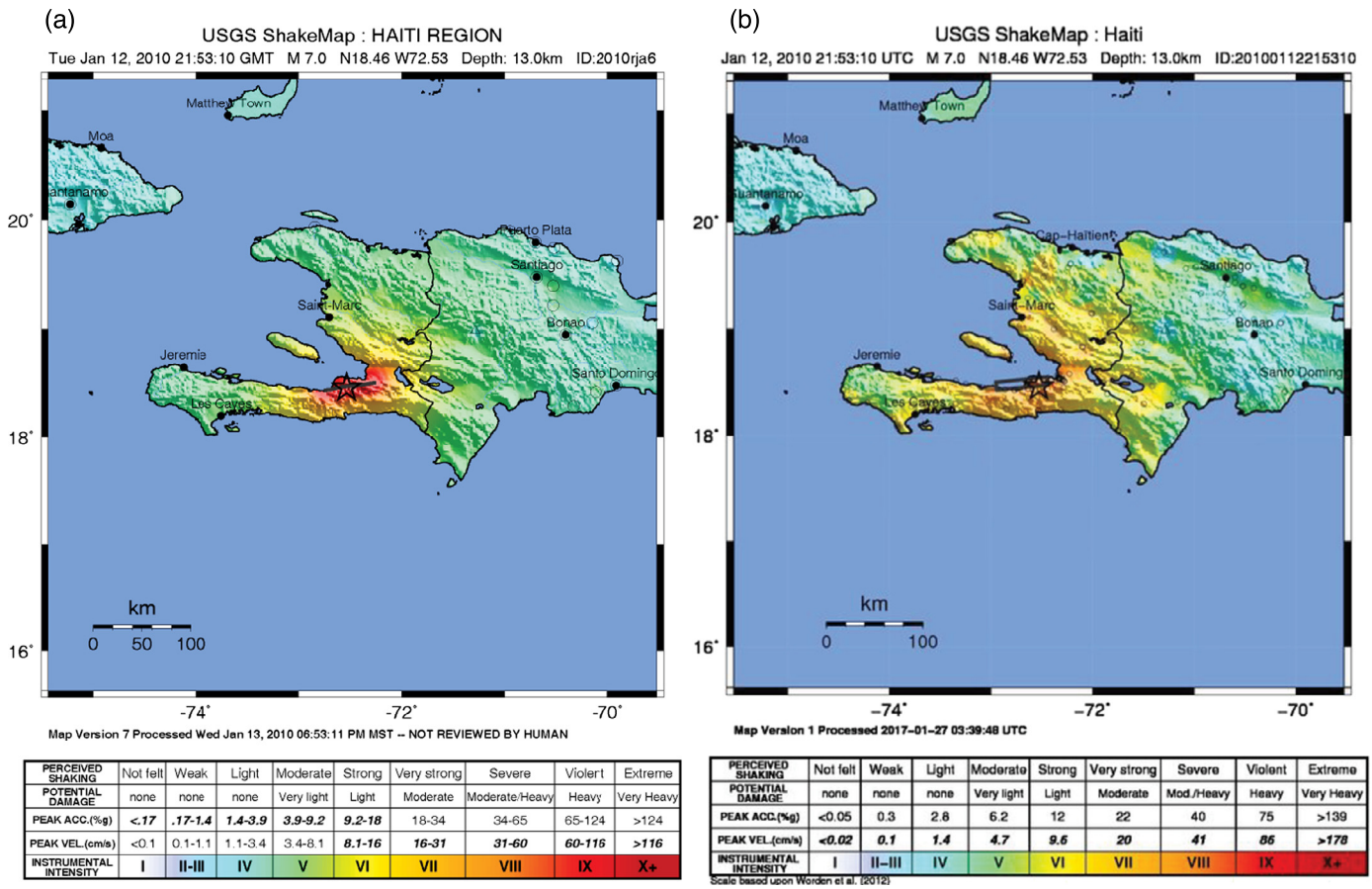

PERCEIVED SHAKING	Not felt	Weak	Light	Moderate	Strong	Very strong	Severe	Violent	Extreme
POTENTIAL DAMAGE	none	none	none	Very light	Light	Moderate	Moderate/Heavy	Heavy	Very Heavy
PEAK ACC.(%g)	*<.17*	*.17-1.4*	*1.4-3.9*	*3.9-9.2*	*9.2-18*	18-34	34-65	65-124	>124
PEAK VEL.(cm/s)	<0.1	0.1-1.1	1.1-3.4	3.4-8.1	*8.1-16*	*16-31*	*31-60*	*60-116*	*>116*
INSTRUMENTAL INTENSITY	I	II-III	IV	V	VI	VII	VIII	IX	X+

PERCEIVED SHAKING	Not felt	Weak	Light	Moderate	Strong	Very strong	Severe	Violent	Extreme
POTENTIAL DAMAGE	none	none	none	Very light	Light	Moderate	Mod./Heavy	Heavy	Very Heavy
PEAK ACC.(%g)	<0.05	0.3	2.8	6.2	12	22	40	75	>139
PEAK VEL.(cm/s)	*<0.02*	*0.1*	*1.4*	*4.7*	*9.6*	*20*	*41*	*86*	*>178*
INSTRUMENTAL INTENSITY	I	II-III	IV	V	VI	VII	VIII	IX	X+

Scale based upon Worden et al. (2012)

Fig. 1. ShakeMaps. (a) The ShakeMap estimated by the USGS approximately one day after the earthquake. (b) A USGS updated ShakeMap compiled on January 27, 2017. (Source: USGS). (For interpretation of the colors in the figure(s), the reader is referred to the web version of this article.)

(Hough et al., 2012), and damage assessment using satellite and aerial imagery as well as surveying damage on the ground (Corbane et al., 2011; Francis et al., 2016). Based on these efforts, the USGS updated the initial ShakeMap estimates to better explain the surveyed damage. The updated ShakeMap in Fig. 1b, compiled by the USGS in January 2017, is much more detailed than the initial ShakeMap that did not incorporate any ground motion measurements nor reported damage.

In addition to seismic waves, earthquakes and underground nuclear explosions generate low-frequency acoustic waves in the atmosphere, known as *infrasound*. Bolt (1964) described exceptional atmospheric waves recorded by a microbarograph in Berkeley, California, after the M_w 9.2 Alaskan earthquake of March 27, 1964, over 3000 km away. Multiple mechanisms play a role in the generation of infrasound waves from a subsurface source.

Arrowsmith et al. (2010) discussed seismo-acoustic coupling mechanisms for earthquakes as well as various other natural and human-made sources. Intuitively, the mechanical disturbance of the ground-atmosphere interface compresses (and decompresses) the atmosphere above and generates an acoustic pressure wave. Physically, boundary conditions require the continuity on normal stress and vertical displacement along the interface. Thus the contribution of the mechanical coupling mechanism to the acoustic pressure perturbation in flat regions, is attributed to seismic waves that contain a vertical component (e.g., P, SV, and Rayleigh). However, steep topography can facilitate coupling of additional phases, even ones that are horizontally polarized as shown by Green et al. (2009).

The ground-atmosphere and ocean-atmosphere interfaces are typically considered to be reflective boundaries to the seismic and acoustic wavefields. However, at low frequencies, this boundary becomes transparent to part of the wavefield (Godin, 2008, 2011) and infrasonic signals can be generated by another, less intuitive mechanism, evanescent wave coupling as observed following the 2004 M_w 8.1 Macquarie ridge earthquake (Evers et al., 2014).

Seismo-acoustic coupled signals can originate from the epicenter (Mutschlecner and Whitaker, 2005), as well as from secondary sources of infrasound away from the epicentral region (Le Pichon et al., 2006; Green et al., 2009; Marchetti et al., 2016). Given an origin time and location, seismo-acoustic signals can be backprojected to locate the point on the Earth's surface at which coupling has occurred. Backprojections of infrasonic signals from earthquakes (Shani-Kadmiel et al., 2018) and nuclear explosions (Assink et al., 2018) provide insight into the seismo-acoustic coupling process and can map the distribution of the epicentral and secondary sources of infrasound. Following the Tohoku earthquake of March 11, 2011, and the Amatrice earthquake of August 24, 2016, ground motions inferred from backprojection were shown to be in agreement with the measured peak surface pressure in the epicentral region (Walker et al., 2013; Hernandez et al., 2018).

Although seismic signals were not measured in Haiti during the 2010 earthquake, infrasound was generated over the region and was detected by an International Monitoring System (IMS) array IS51 on Bermuda island, 1738 km away (Fig. 2). In what follows, we first use array processing to resolve plane-wave parameters of the infrasonic signals detected in Bermuda (Fig. 3). Next, we examine the generation and propagation of infrasound from the earthquake source in the subsurface (Fig. 4). We then use the resolved wavefront parameters and atmospheric propagation conditions to backproject the detections and map the acoustic intensity mea-

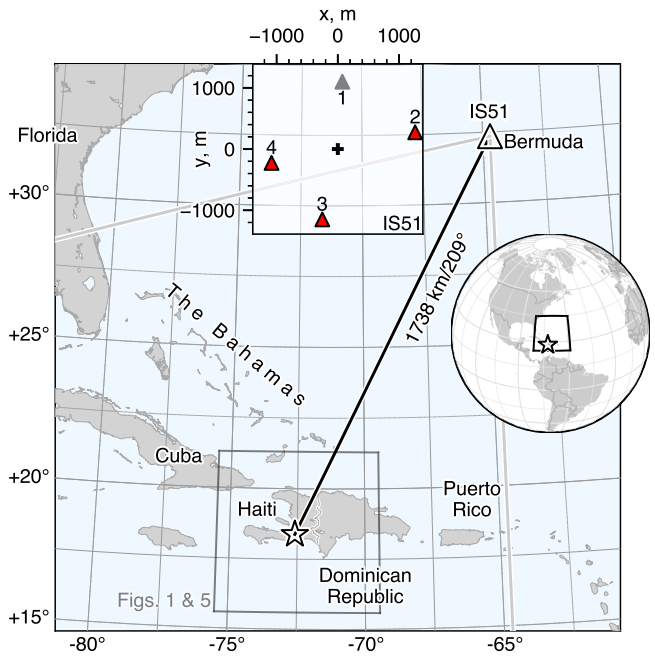

Fig. 2. Overview map showing the epicenter (star) and infrasound array IS51 on Bermuda island (triangle). The great circle path connecting IS51 with the epicenter measures 1738 km long with theoretical back azimuth of 209°. The bounds of the back azimuth range used for beamforming are indicated in gray. The array configuration of IS51 is shown in inset frame.

sured at IS51 to source patches in the epicentral region (Fig. 5a). In addition, we are able to detect the ground motion polarity of the compressional and dilatational quadrants around the epicenter (Fig. 5b). This observation is supported by a simulation of an extended infrasound source using the *Rayleigh integral* (Fig. 6).

2. Data acquisition and beamforming results

IS51 is a four-element array located on Bermuda island, situated 1738 km from the epicenter in Haiti (Fig. 2a). The array is equipped with MB2005 microbarometric sensors that have a flat frequency response between 0.01 and 27 Hz. A rosette wind-noise reduction system is used to reduce wind noise over the infrasonic frequency band by spatially averaging the pressure field in the vicinity of each infrasound sensor (Hedlin and Raspet, 2003; Gabrielson, 2011). The pressure field is continuously recorded at a rate of 20 samples-per-second, and the waveform data are detrended, tapered, and band-pass filtered before time-domain beamforming (Fig. S1 in Supplementary material). A second-order Butterworth band-pass filter between 0.45 and 2 Hz is chosen to reduce interference from low-frequency signals in the microbarom band as well as higher frequency wind-noise.

A time-domain beamforming technique (Melton and Bailey, 1957) is used for the detection of coherent infrasound and the estimation of plane-wave parameters. It is a delay-and-sum technique that enhances coherent signals and suppresses the incoherent background noise. Consequently, coherent signals with amplitudes below the background noise levels can be detected. A detection is based on the evaluation of a Fisher ratio (F_r), which corresponds to the signal-to-noise ratio (SNR): $F_r = N \cdot \mathrm{SNR}^2 + 1$, where N is the number of array elements (Melton and Bailey, 1957).

The waveform data are processed in time-windows T_w of 30 seconds with 99% overlap between successive windows. A large overlap yields detections with a high temporal resolution and is beneficial for the backprojection algorithm. The samples are delayed and summed over a horizontal slowness grid. The grid is designed to include back azimuth and apparent velocity values of interest. The back azimuth values range between 180° and 260° and are spaced by 1°. This range is selected to avoid detection of microbarom sources in the Atlantic. The apparent velocity values range between 0.28 km/s and 6 km/s. Between 280 and 450 m/s (the infrasonic signal range), the values are evenly spaced by 5 m/s, and between 450 m/s and 6 km/s (the seismic signal range), the spacing increases logarithmically from 16 to 200 m/s. This yields 8829 slowness vectors that are evaluated at each of the 26,700 processing time-windows. We used only three out of the four elements due to anomalous high noise levels at H1 (see Fig. S1 in Supplementary material), likely due to a malfunctioning wind-noise reduction system.

Characteristic wavefront parameters are extracted in the beamforming process, namely, the direction of arrival *back azimuth* (BAZ), the speed of horizontal propagation over the array *apparent velocity* (AV), and the signal coherency in terms of SNR (Fig. 3c-e, respectively). Generally, epicentral infrasound signals are empirically characterized by a *celerity* (epicentral distance divided by the total travel-time) range of 0.34 to 0.31 km/s for stratospheric propagation and 0.31 to 0.28 km/s for thermospheric propagation (Evers and Haak, 2007). However, coherent signals (SNR > 0.7) are only detected between ~5500 and ~6100 seconds (celerity range of 0.32 to 0.28 km/s), mostly corresponding to the thermospheric celerity range. The right column in Fig. 3 focuses on detections that correspond to infrasound signals from the epicentral region. Only detections that fit our selection criteria (200° < BAZ < 220°, 320 < AV < 400 m/s, and SNR > 0.7) are shown. These are later used in the backprojection process. Inclination angles measured up from the horizontal are calculated using the relation $\phi = \arccos(c/\mathrm{AV})$, where c=342 m/s is the local speed of sound (assuming zero wind) at IS51 and AV is the observed apparent velocity for each detection. This yields observed inclination angles from 7° to 25°.

3. Seismo-acoustic coupling and propagation from Haiti to Bermuda

Waveguides in the atmosphere facilitate long-range infrasound propagation and its detection at ground-based stations (Waxler and Assink, 2019). These waveguides are defined by temperature and wind gradients that refract part of the acoustic wavefield back toward the ground. The typical atmospheric waveguides, classified by the layers of the Earth's atmosphere, are the tropospheric, stratospheric, and thermospheric waveguides. In the troposphere and stratosphere, the adiabatic speed of sound is usually insufficient to form waveguides. Therefore, wind in the direction of propagation is essential to facilitate ground-to-ground propagation. This dependence on wind limits sound propagation in specific directions.

In the troposphere, propagation is typically not efficient over long-ranges (distances of more than 100 km) due to the relatively limited size of the jet stream. In the stratosphere, advantageous conditions by the much larger circumpolar vortex support efficient propagation over very long-ranges (Waxler and Assink, 2019) (distances exceeding 2000 km), though, stratospheric winds are significantly varying on a (sub)seasonal scale. In the thermosphere, the temperature gradient alone is sufficient to refract infrasound to the ground regardless of propagation direction. However, long-range propagation is less efficient compared to a stratospheric waveguide due to the higher attenuation in the thermosphere (Sutherland and Bass, 2004).

In a horizontally layered atmosphere, the first-order effects of temperature and horizontal wind in the direction of propagation are approximated by the *effective speed of sound* c_{eff} (Godin, 2002). Following Snell's law, the horizontal component of the speed of

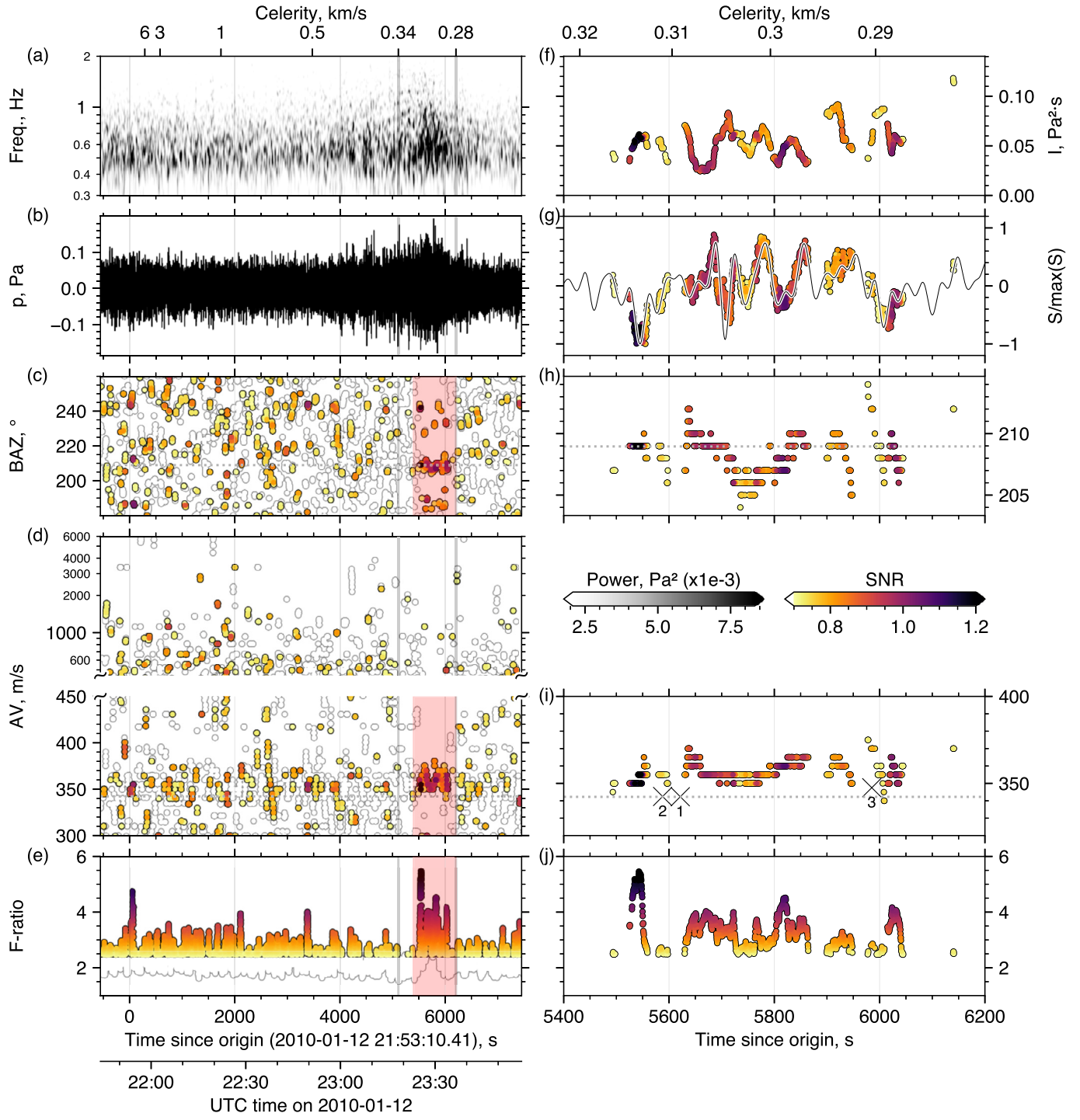

Fig. 3. Beamforming results. The left column summarizes all beamforming results. (a) The spectrogram of the best beam (gray scale indicating power is shown to the right of (d)). (b) The best beam. Subsequent frames show the following wavefront parameters as retrieved in each time-window: (c) Back azimuth (BAZ; true back azimuth indicated by dotted gray line), (d) Apparent velocity (AV; local speed of sound indicated by dotted gray line), and (e) Fisher ratio (F-ratio). Vertical gray lines indicate the expected time range of epicentral infrasound. The red box indicates the enlarged range plotted in the right column. The right column focuses on the epicentral infrasound detections that are used in the backprojection algorithm. (f) Acoustic intensity I used to scale the detections in the backprojection algorithm for Fig. 1c. (g) Normalized sum of the pressure used to scale the detections in the backprojection algorithm for Fig. 1d. The best beam, low-pass filtered to 1/30 Hz and normalized, is also plotted. (h-j) same as (c-e). X-symbols in frame (i) correspond to the travel-time and apparent velocity of calculated eigen rays plotted in Fig. 4. The color scale indicates the SNR of the detection. Travel time in seconds since origin time and UTC time are indicated on the bottom axis and celerity (average horizontal propagation velocity) is indicated on the top axis.

propagation (referred to as AV in section 2) remains constant while crossing between layers. Therefore, a negative gradient in the c_{eff} profile causes the wave to refract upward, and a positive gradient causes the wave to refract downward. At the return height of the wave, the AV of the wave and the c_{eff} in the medium are equal. The c_{eff} profile, therefore describes, to first-order, the part of the acoustic wavefield that can get trapped in the atmospheric waveguides and thus contribute to long-range propagation. Furthermore, return heights are thus constrained to the parts of the c_{eff} profile that exceed the initial velocity at the ground (c_{eff} ratio > 1) in

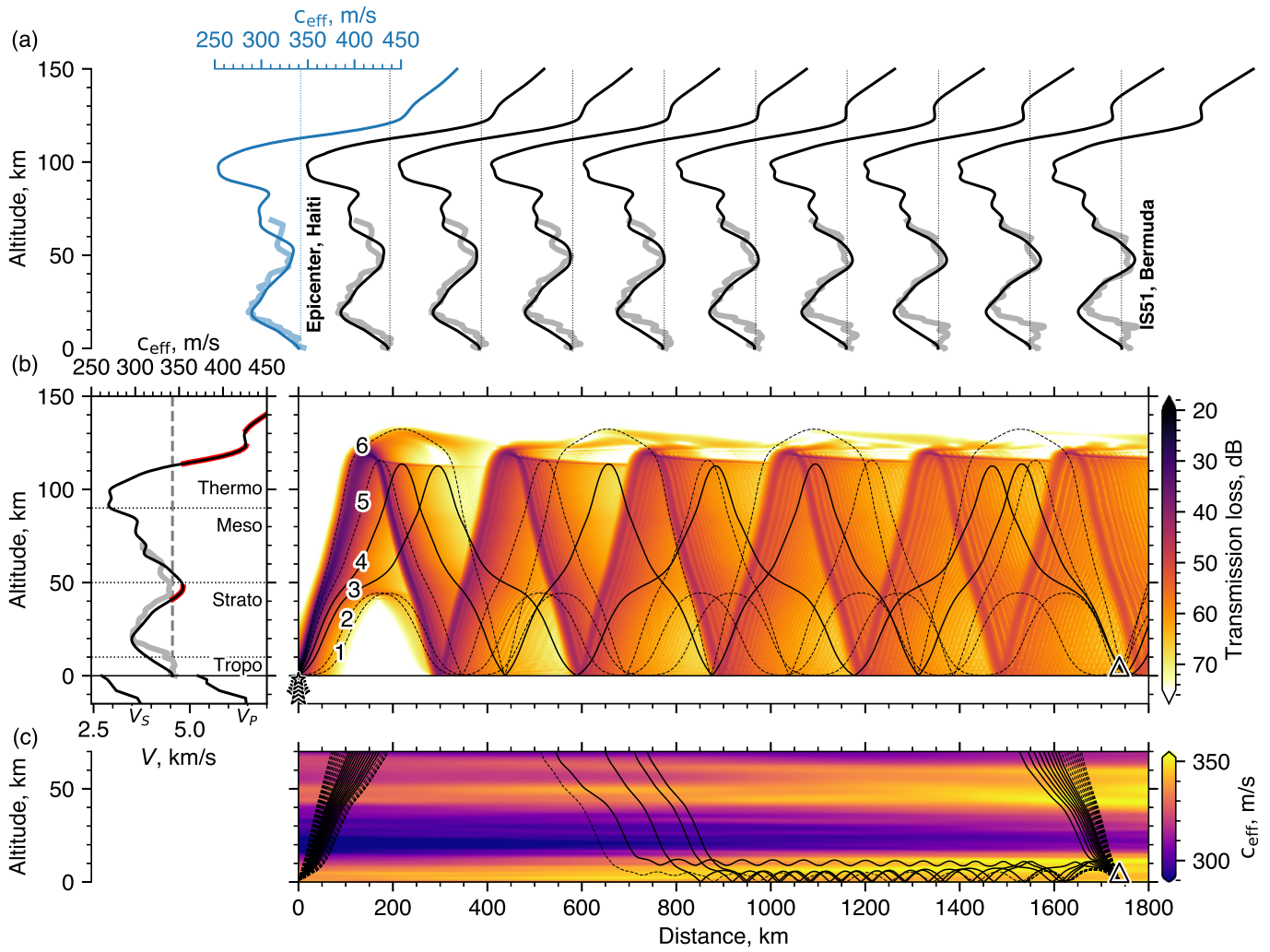

Fig. 4. Coupling and propagation modeling. (a) 10 evenly spaced effective sound speed profiles along the great circle path connecting the epicenter in Haiti to IS51 on Bermuda. Top axis shown for scale and indicates c_{eff} of the leftmost profile. The climatology profiles are indicated by thin black lines, the ERA5 ECMWF profiles are indicated in thick gray lines. (b, left) Averaged effective speed of sound profile (values on the top axis) and seismic velocity profile (values on the bottom axis) used in the FFP and c_{eff} ray tracer. Vertical dashed line indicates c_{eff} at ground level and regions of potential return height for a c_{eff} ratio > 1 relative to the previous waveguide are outlined in red. Horizontal dotted lines indicate boundaries between troposphere, stratosphere, mesosphere, and thermosphere. For comparison, the ERA5 ECMWF profiles are also averaged and plotted as thick gray line. (b, right) Vertical section showing acoustic intensity transmission loss (TL) along the propagation path from a subsurface source in Haiti to IS51 on Bermuda island. The sources are indicated by stars with size corresponding to relative source magnitude. IS51 is indicated by a triangle. Eigen rays connecting the source region and IS51 calculated using the same c_{eff} profile are overlaid. (c) Vertical cross section of effective sound speed calculated from ERA5 ECMWF specifications showing rays back-propagated along the theoretical back azimuth ±15°. Solid lines indicate rays corresponding to the observed range of inclination angles (7° - 25°) and dashed lines indicate rays outside that range.

the case of a single waveguide or that of the waveguide below in the case of multiple waveguides. Depending on the direction of the wind with respect to the direction of propagation, multiple waveguides can co-exist.

The part of the wavefield consisting of high apparent velocities, which correspond to steeper angles of propagation, do not become trapped in the atmospheric waveguides and are not returned to the ground. In particular cases, these signals can be detected by satellites in low earth orbits. For instance, at 270 km altitude, the GOCE mission detected density variations and vertical displacements created by post-seismic infrasound from the Tohoku earthquake of March 11, 2011 (Garcia et al., 2013).

For the analysis of infrasound propagation conditions at the time of the earthquake, empirical atmospheric models, known as *climatologies*, for temperature (MSIS-00 (Picone et al., 2002)) and horizontal wind (HWM14 (Drob et al., 2015)) are compared with actual conditions provided by the high-resolution ERA5 reanalysis from the European Centre for Medium-Range Weather Forecasts (ECMWF) (Fig. 4a). The resulting c_{eff} profiles from these, differ in two waveguides: (1) In the troposphere, a weak tropospheric duct is present in the ECMWF profiles, which is unresolved in the climatology. However, as mentioned above, this waveguide does not sustain long-range propagation and acts as a filter that prevents lower apparent velocities from reaching higher ducts. (2) The stratospheric waveguide is weaker than in the climatology and weaker than the tropospheric waveguide, potentially creating an elevated duct. This effect strengthens over Bermuda and therefore makes it unlikely to detect stratospheric returns according to the atmospheric conditions of ECMWF.

A Fast Field Program (FFP) (Averbuch et al., 2020a) is utilized to simulate long-range infrasound propagation from a subsurface source in Haiti to IS51 on Bermuda island. The FFP is a coupled seismo-acoustic solver that provides an exact solution for wave propagation in layered media in the frequency-wavenumber (f-k) domain. Within each layer, an exact solution of the wave equation describes the propagating waves, and the layers are coupled by the boundary conditions, i.e., continuity of stress and displacement. This form of solution supports the simulation of wave prop-

agation through stark discontinuities in the density and velocity profiles like the ground-atmosphere and ocean-atmosphere interfaces (Averbuch et al., 2020a,b).

Seismo-acoustic coupling is governed by three parts of the seismic wavefield spectrum. (1) Homogeneous body waves, (2) Inhomogeneous (evanescent) body waves, and (3) Surface waves. However, only the parts of the wavefield that consist of apparent velocities that can get trapped in the atmospheric waveguides contribute to long-range propagation and are of interest in our modeling. Moreover, these waves undergo enhanced sound transmission across the ground-atmosphere interface, generating infrasonic signals with larger amplitudes than expected (Godin, 2011).

The computational domain consists of coupled solid-fluid media: In the subsurface, seismic velocities V_P and V_S correspond to the structure of the upper crust below Haiti (Possee et al., 2019). In the atmosphere, ten evenly spaced climatology profiles are averaged along the great circle path from Haiti to Bermuda (Fig. 4b, left) to define the c_{eff} profile used in the FFP simulations (Fig. 4b, right).

Source slip inversions from teleseismic data show that slip was distributed between the hypocenter, at a depth of 13 km, and 2 km depth, with the largest slip occurring at a depth of 10 km (Hayes et al., 2010). To account for this distribution, pressure-wave propagation is initiated by five evenly spaced point sources with magnitude decreasing as a function of the square root of the vertical distance from 10 km to 2 km depth (Fig. 4b, right). The simulated frequency is 0.5 Hz, and phase velocities are bound between 280 m/s and 450 m/s, corresponding to the infrasonic signal range in the beamforming process. This also corresponds to the effective speed of sound range that can become trapped in the atmospheric waveguides. The pressure field resulting from each source is stacked and the acoustic intensity (I) is calculated as $I = p^2/(\rho \cdot c_{eff})$, where p is the pressure, and ρ is the density. The transmission loss (TL) is calculated as $\text{TL} = -10\log_{10}(I/I_0)$, where I_0 is the acoustic intensity just above ground over the source. In this study we assume a lossless propagation medium in which attenuation is only due to geometrical spreading.

Fig. 4b (right) shows the infrasound propagation from sources in the subsurface under Haiti to Bermuda in terms of TL. For simplicity, the values in the subsurface are masked. Return heights correspond to the parts of the c_{eff} profile that are outlined in Fig. 4b (left), where the c_{eff} ratio > 1 relative to the ground or the previous waveguide.

In addition, the averaged c_{eff} profile is used to calculate ray paths in a one-dimensional (1D) layered windless atmosphere. Eigen rays connecting the epicenter and IS51 are shown in Fig. 4b. Eigen rays 1, 2, and 3 fit the observations in terms of the travel-time with values of 5621, 5588, and 5985 seconds, respectively, but only ray number 3 is within the observed inclination angle range (see section 2 and Fig. 3i). Recalling that the averaged c_{eff} profile, which is based on climatology data, differs from the ECMWF profiles, it is unlikely that eigenrays 1 and 2 would have propagated to Bermuda; they would either get trapped in the tropospheric waveguide and decay or become trapped in the elevated duct over Bermuda. Ray 4 is also within the observed inclination angle range but rays 4, 5, and 6 have theoretical travel-time values beyond the observed range of coherent detections (6322, 6715, and 6136 seconds, respectively).

To model propagation paths in further detail and investigate the inclination range of possible rays incoming to IS51, we propagated rays using an in-house developed ray tracing algorithm, cast in spherical coordinates, that accounts for the full effect of the three-dimensional (3D) inhomogeneous wind and temperature fields (see section 2.2 in Smets (2018)). For the forward propagation (see rays on the left side of Fig. 4c), we used the high-resolution ERA5 ECMWF atmospheric specifications provided for 22:00 UTC (~7 minutes after the earthquake's origin time). Rays are launched at the epicenter toward IS51 over an azimuth range of ±15° of the theoretical azimuth at 0.5° azimuthal spacing and at inclination angles of 0° to 40° every 0.5° above the horizontal. For the back propagation (see rays on the right side of Fig. 4c), we used the atmospheric specifications provided for 23:00 UTC. Rays are launched at the central coordinates of IS51 toward the epicenter over an azimuth range of ±15° of the theoretical back azimuth at 0.5° azimuthal spacing and at inclination angles of 0° to 40° every 0.5° above the horizontal. In order to facilitate backward propagation, the horizontal components of the wind are reversed.

In the forward propagation case, rays propagate steeply upward through the troposphere and stratosphere and exit through the top boundary due to the weak tropospheric duct and even weaker stratospheric duct over Haiti. In the back propagation case, rays with inclination angles below 14.5° remain trapped in the troposphere until the waveguide is weak enough to escape. Rays with inclination angles above 14.5° have a high enough apparent velocity to propagate through the troposphere, but are not trapped by the stratosphere and continue upward. In either case, the stratospheric waveguide in the ERA5 ECMWF specifications is too weak to refract these rays back toward the ground. It is therefore assumed herein that infrasound propagation from Haiti to Bermuda was facilitated by a thermospheric waveguide.

4. From detections in time to acoustic intensity map

The severity of ground shaking generally decreases with distance from the epicenter, however, near-surface geology, topography, and the source radiation pattern, contribute to local variations in ground shaking intensity. This variability is captured by the coupled acoustic pressure field over the disturbed region (Walker et al., 2013). Given that the wave is most sensitive to the atmosphere at the return height (Assink et al., 2019) and that the epicentral infrasound propagation was facilitated by a thermospheric waveguide, it is valid to assume that the atmosphere is constant throughout the duration of the detected signal (~600 seconds in Fig. 3). Thus the radiated signals from the different sub-patches in the near-source region remain ordered in time throughout the propagation from the epicentral region to Bermuda, and the variability of acoustic pressure perturbations from one location to another can be retrieved.

The backprojection algorithm makes use of the travel-time and back azimuth associated with each detection time-window to map detections in time to their point of origin on the Earth's surface. Building on the backprojection algorithm outlined in Shani-Kadmiel et al. (2018), corrections for advection effects are incorporated. Each cell in the grid-search domain is prescribed a back azimuth and infrasound propagation velocity correction values, which are derived from the cross-track and along-track winds. Furthermore, uncertainties with regard to the time of detection and back azimuth are treated; the time of a detection is assumed to be at the center of each processing time-window however, a detection can appear anywhere within the detection window. This uncertainty translates to a spatial error in the along-track direction that amounts to $\pm T_w \cdot c_i/2$ (~5 km for 30 second-long processing windows T_w and infrasound celerity c_i of ~0.3 km/s). Additionally, uncertainty in the detection's back azimuth due to the resolution of the beamforming (1°), translates to a spatial error in the cross-track direction. In contrast to the detection time uncertainty that translates to a constant along-track spatial error size, the size of the spatial error in the cross-track direction due to the back azimuth uncertainty grows with receiver-source (backprojection) distance. For example, at the epicenter, 1738 km away from IS51, this error amounts to ~±15 km. In this study, we assume

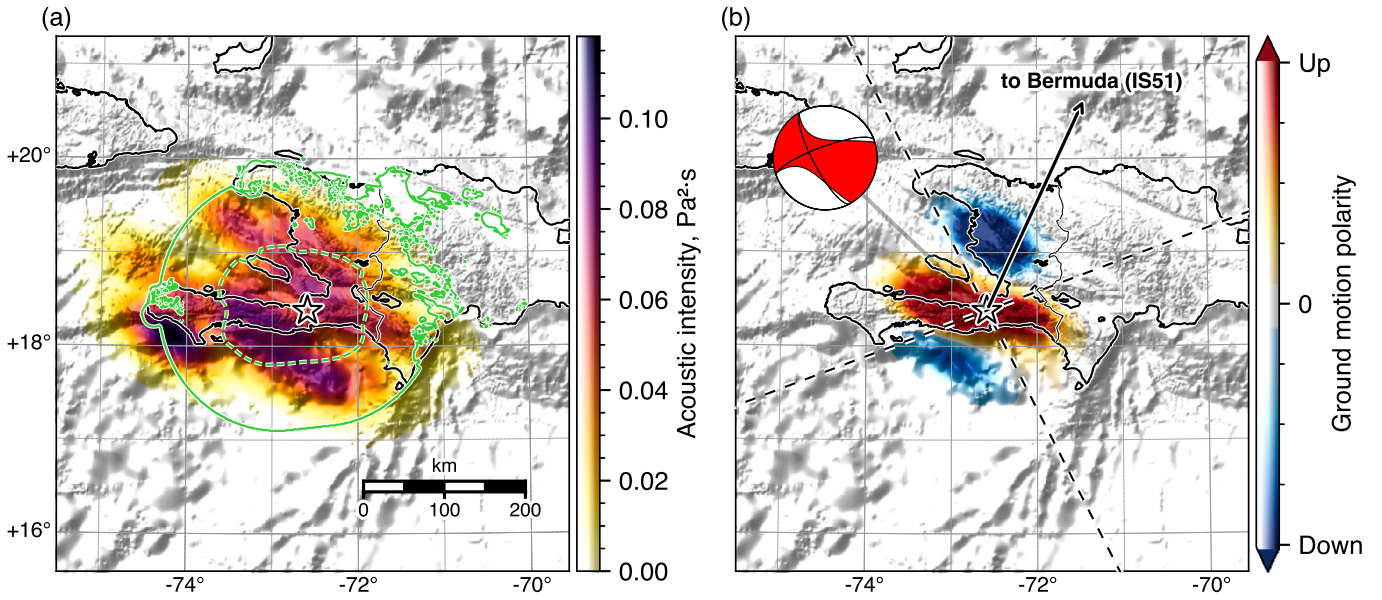

Fig. 5. (a) Acoustic intensity map from backprojection of infrasound detections showing the acoustic intensity I measured at IS51 mapped onto the source region. The I_I = 5 contour lines from the initial (broken line) and updated (solid line) USGS ShakeMaps (Fig. 1) are overlaid in green. (b) Source radiation pattern from backprojection of infrasound detections, red indicates upward motion, blue indicates downward motion. The beachball representation of the moment tensor (Nettles and Hjörleifsdóttir, 2010) and nodal planes are overlaid. The direction to IS51 on Bermuda island is indicated by an arrow (~45° to the nodal planes).

these spatial uncertainties to have a Gaussian distribution around the resolved location for each detection, resulting in a detection patch.

The *acoustic intensity* I associated with each detection window i at time t_d with start time $t_0 = t_d - T_w/2$ and end time $t_1 = t_d + T_w/2$ is calculated as $I_i = \sum_{t_0}^{t_1}(p^2)dt$, where T_w is the processing time-window length, p is the pressure, and dt is the temporal resolution of the signal (Fig. 3f). As a detection window in time is mapped to a detection patch in space, this value is used to estimate the acoustic intensity associated with the part of the signal that was contributed by that patch. The region outlined in the acoustic intensity map (Fig. 5a), covers a much larger extent than the initial USGS ShakeMap estimates (Fig. 1a). For comparison, the region where shaking intensity was sufficiently strong to cause damage is outlined by the *instrumental intensity* I_I = 5 contour line, extracted from the updated USGS ShakeMap estimates (Fig. 1b). The same contour line from the initial USGS ShakeMap (Fig. 1a) outlines a much smaller region. In both cases, The USGS ShakeMaps, as well as our acoustic intensity map, are models. And even though our acoustic intensity map and the updated ShakeMap do not perfectly overlap, they both provide a better representation of the geographical extent of the observed damage.

5. Source radiation map

Similarly, the pressure-time integral (S) in each detection window is calculated as $S_i = \sum_{t_0}^{t_1}(p)dt$ and yields a positive or negative overall pressure sum (Fig. 3g); This indicates whether the detection patch mostly moved upward or downward. It is noted that these values follow the lowpassed best beam trace (Fig. 3g). The resolved radiation pattern in Fig. 5b outlines three distinct regions. The two blue patches reflect an overall downward motion and coincide with the dilatational quadrants depicted by the earthquake moment tensor (Nettles and Hjörleifsdóttir, 2010). The red patch in the middle reflects an overall upward motion and is smeared across the compressional quadrants.

To better understand this result, a conceptual model is set up to simulate the acoustic pressure field from an extended infrasound source, as illustrated in Fig. 6a. In a homogeneous half-space, the radiated acoustic pressure field, $p(\boldsymbol{r}, \omega)$, from a planar vibrating surface can be computed by the Rayleigh integral (Wapenaar and Berkhout, 1989; Green et al., 2009):

$$p(\boldsymbol{r}, \omega) = \frac{ik\rho c}{2\pi} \int_{S_0} \frac{e^{-ik|\boldsymbol{r}-\boldsymbol{r}_0|}}{|\boldsymbol{r}-\boldsymbol{r}_0|} v(\boldsymbol{r}_0, \omega) dS_0, \tag{1}$$

where $\boldsymbol{r} = (x, y, z)$ is a receiver location, $\boldsymbol{r}_0$ is a location on the vibrating surface, ω is angular frequency, k is the medium wavenumber, $v(\boldsymbol{r}_0, \omega)$ is the complex spectral component of the surface vertical velocity, and the kernel, $\exp(-ik|\boldsymbol{r}-\boldsymbol{r}_0|)/|\boldsymbol{r}-\boldsymbol{r}_0|$, is the Green's function for a homogeneous medium.

In this study we use a Gaussian pulse STF

$$v(\boldsymbol{r}_0, t) = \frac{\omega_0}{\sqrt{2\pi}} e^{-\omega_0^2 (t-t_0)^2/2}, \tag{2}$$

with a central frequency ω_0 = 0.1 Hz to drive the source velocity, which when integrated, describes the permanent displacement (see Section 2 of the Supplementary material). Using the Fourier transform, the spectral components of the STF are represented as:

$$v(\boldsymbol{r}_0, \omega) = \int_{-\infty}^{\infty} v(\boldsymbol{r}_0, t) e^{-i\omega t} dt, \tag{3}$$

and the waveforms at the receiver are obtained by the inverse transform

$$p(\boldsymbol{r}, t) = \frac{1}{2\pi} \int_{-\infty}^{\infty} p(\boldsymbol{r}, \omega) e^{i\omega t} d\omega. \tag{4}$$

To evaluate the integral, the surface is discretized into individual pistons with a 400 m radius (example code is provided Section 2 of the Supplementary material).

Pistons in the top-left and bottom-right quadrants (first and third) are prescribed a positive (upward) STF, and pistons in the top-right and bottom-left quadrants (second and fourth) are prescribed a negative (downward) STF (Fig. 6a). The activation of each

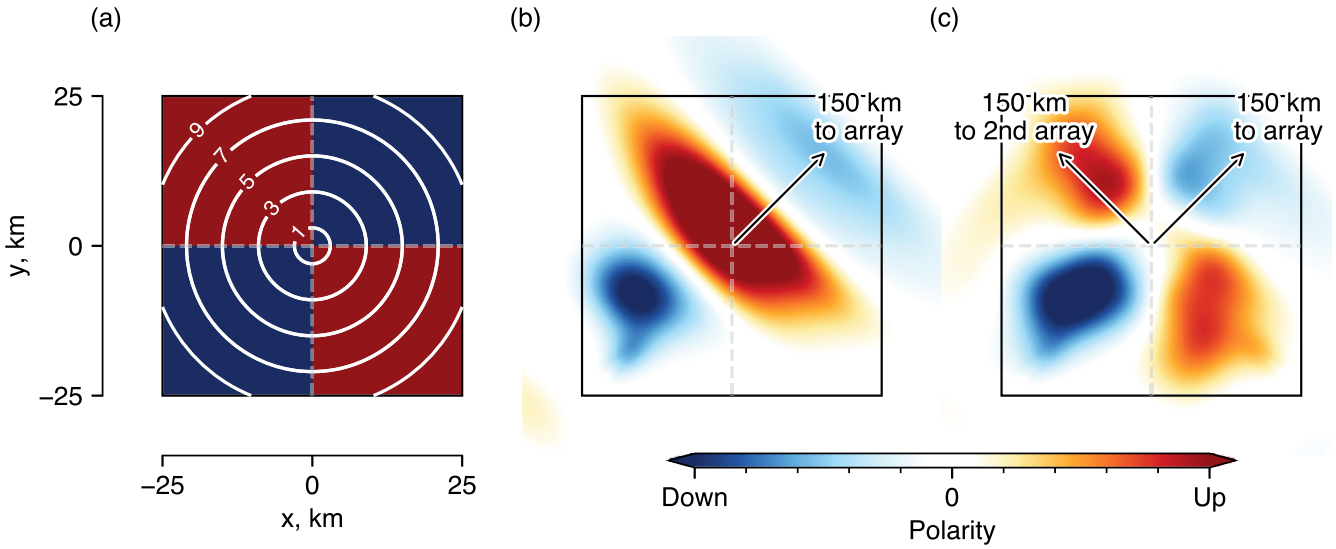

Fig. 6. Extended source modeling and backprojection. (a) Extended source setup with four quadrants: red indicates upward motion, blue indicates downward motion. White contour lines indicate isochrons of piston activation time in seconds. (b) Source radiation pattern inferred from backprojection of synthetic infrasound signals using one array located 150 km away from the epicenter, 45° to the nodal planes in the direction indicated by the arrow. (c) Superposition of source radiation patterns inferred from backprojection of synthetic infrasound signals using two arrays located 150 km away from origin at 45° to the nodal planes in the direction indicated by the arrows.

piston is offset in time to mimic a radially propagating seismic wave with a moveout velocity of 3 km/s from the simulated epicenter at the center of the extended source.

Synthetic waveforms are calculated for a four-element array in the far-field, 150 km away from the epicenter at 45° to the nodal planes to mimic the orientation of IS51 with respect to the nodal planes of the Haiti earthquake. Wavefront parameters are extracted in a beamforming process, as described in Data acquisition and beamforming results, and then used in the backprojection process. The pressure-time integral S in each detection window is used to infer the ground motion polarity of each detection patch.

As before, three distinct patches are resolved (Fig. 6b) with the middle patch smeared across compressional quadrants one and three. The source-receiver distance in the synthetic model is three-times the width of the extended infrasound source and roughly five-times the width of the observed infrasound source in the case of the Haiti earthquake (Fig. 5b). Recalling that the size of the spatial error in the cross-track direction grows with distance from the receiver, it is clear why these quadrants become merged in the backprojection process. We repeat the process to simulate waveforms at a second array at -45° to the nodal planes. Since the travel-time and back azimuth detected at one array are independent of those detected at another array, the backprojection process can be carried out independently per array and the results can be combined in several ways (Hernandez et al., 2018). Here, because of the simplicity of the source and the fact that each piston moves either up or down with no further oscillations, we can stack and average the two source radiation maps and resolve the polarity in each of the four quadrants (Fig. 6c).

6. Discussion and conclusions

Following the 2010 Haiti earthquake, infrasound was detected at an IMS station on Bermuda island. Although a glance at the waveforms in Fig. S1 (Supplementary material) might not be encouraging, we were able to extract coherent signals that are well within the level of the background noise and associate these with the epicentral region in Haiti using wavefront parameters extracted in the beamforming process (Fig. 3). Two seismo-acoustic coupling mechanisms and their contribution to infrasound generation over the source region are discussed: (1) our FFP simulations indicate that energy from sources in the subsurface, evanescently coupled to the atmosphere and generated infrasound (Fig. 4), and (2) extended infrasound source modeling demonstrates that the mechanical coupling process, that is, the perturbation of the acoustic pressure field in response to shaking of the ground-atmosphere interface, preserves the ground motion polarity that is determined by the faulting mechanism (Fig. 6).

Our analysis of the atmospheric propagation conditions included climatological profiles as well as high-resolution ERA5 ECMWF atmospheric specifications. From this analysis it followed that propagation of infrasound was most likely facilitated by a thermospheric waveguide (Fig. 4). This is further supported by the celerity range and the clean wave train (single-duct waveform, no multipathing signature) of the observed infrasound detections. In fact, if instead of calculating the celerity with respect to the horizontal distance to the epicenter we correct for the horizontal distance to the detection patch, the celerity values remain below 0.3 km/s. Infrasound propagation modeling through the thermosphere remains a challenge as wind and temperature specifications are, for the most part, limited to climatological averages. Such models do not yet accurately describe this region of the atmosphere that is characterized by large diurnal variations in wind and temperature due to (non-linear interactions between) atmospheric tides and (breaking) gravity waves (Drob et al., 2015; Blanc et al., 2017; Assink et al., 2019). In addition, non-linear propagation effects, absorption of infrasound as well as the interplay between these two aspects are significant in the upper atmosphere (Lonzaga et al., 2015) and not well understood.

Backprojections of infrasound signals have been shown to be in correlation with earthquake ground motions prior to this work but for shorter propagation ranges and only for stratospheric infrasound (Marchetti et al., 2016; Walker et al., 2013; Hernandez et al., 2018). For the first time, infrasound that has propagated over 1700 km is used to outline the region where shaking intensity is sufficiently large to lead to damage (Fig. 5a). In addition to shaking on land, our backprojection illuminates sources of infrasound over the ocean in the epicentral region. Infrasound from these sources evanescently coupled from shaking of the ocean floor. Furthermore, ground motion polarity in the epicentral region is resolved (Fig. 5b). This provides an unprecedented insight into earthquake

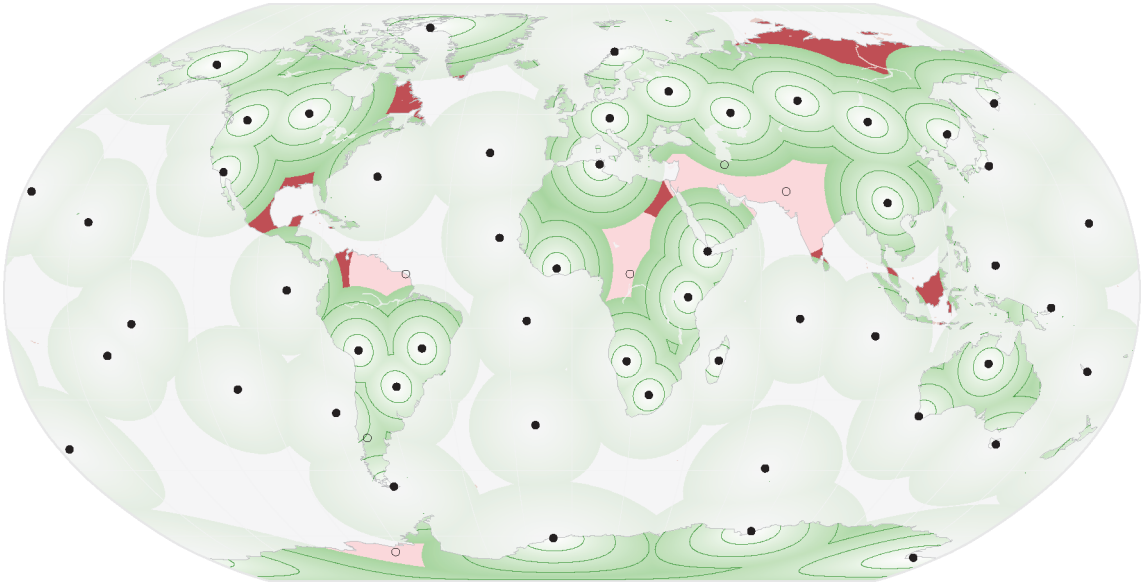

Fig. 7. Acoustic intensity map potential of the IMS. The green gradient shading indicates coverage of the currently installed infrasound stations (full circles). Green shading corresponds to distance out to 2000 km. Contour lines spaced 30 minutes apart indicate travel-time to the nearest station, calculated on the basis of thermospheric propagation. The light red shading indicates regions that will be covered by planned stations (empty circles). Dark red regions correspond to landmass that will remain uncovered by the IMS for this application.

source characterization based on infrasound detections at ground-based stations in the far-field.

In this study, we demonstrate the potential of remote infrasound detections for mapping the acoustic intensity over an earthquake source region. We defer derivation of absolute ground motions in terms of peak ground velocity or acceleration to future studies that should: (1) account for the propagation term in a more precise manner, and (2) compare measured ground motions in the near-source region with derived ground motions from back-projections. Such derivations can then be incorporated as another information layer in the ShakeMap generation process.

Infrasound technology is part of the IMS, a global network for the verification of the Comprehensive Nuclear-Test-Ban Treaty (CTBT) (Dahlman et al., 2009). Currently, 52 out of 60 IMS infrasound arrays are operational and streaming data in real-time to the International Data Center in Vienna. Considering a 2000 km radius around each station, the total landmass coverage by at least one station is 90% with an additional 7% that will be covered once the network is complete (Fig. 7). Large regions are covered by more than one station. Other infrasound stations, known to provide additional coverage, can be incorporated. These include the USArray-Transportable-Array (TA) stations equipped with a microbarometer alongside each seismometer since 2007, stations of the ARISE (Blanc et al., 2017) (Atmosphere dynamics Research InfraStructure in Europe) initiative, and other nationally operated infrasound stations (Pilger et al., 2018).

Nippress and Green (2019) have shown that infrasound propagation in a thermospheric waveguide is effective out to a range of 2000 km with celerity values around 0.28 km/s. The expected infrasound travel-time over 2000 km assuming a thermospheric waveguide is approximately 2 hours under typical propagation conditions. This means that an acoustic intensity map can be produced faster than other methods such as damage analysis on the ground or from aerial and satellite imagery. This can be done for earthquakes almost anywhere on land or close to shore. The techniques presented here, together with the coverage extent, make it plausible to use infrasound as a global earthquake disaster mitigation technique for the first time.

CRediT authorship contribution statement

Shahar Shani-Kadmiel: Conceptualization, Methodology, Project administration, Software, Visualization, Writing – original draft. **Gil Averbuch:** Methodology, Software, Writing – review & editing. **Pieter Smets:** Methodology, Software, Visualization, Writing – review & editing. **Jelle Assink:** Methodology, Software, Writing – review & editing. **Läslo Evers:** Funding acquisition, Supervision, Writing – review & editing.

Declaration of competing interest

The authors declare that they have no known competing financial interests or personal relationships that could have appeared to influence the work reported in this paper.

Acknowledgements

The infrasound data used for this article are provided by the Comprehensive Nuclear-Test-Ban Treaty Organization (CTBTO) and are available to member states. Data can be requested for academic purposes via the virtual Data Exploration Center (vDEC). The CTBTO and International Monitoring System (IMS) station operators are thanked for the high-quality data and products. The high resolution ERA5 Climate Reanalysis data is freely available via the Copernicus Climate Change Service (C3S) Climate Data Store (CDS). Figures in this article (1-6) are made with Matplotlib (Hunter, 2007) and (7) The Generic Mapping Tools (Wessel et al., 2019). We thank reviewer Susan Hough and an anonymous reviewer for their thorough and constructive reviews of the manuscript. We also thank Kees Wapenaar, Auke Barnhoorn, and Thomas Reinsch for their pre-submission review and discussions.

Funding: The contributions by Shahar Shani-Kadmiel, Pieter Smets, and Läslo Evers are funded through a VIDI project from The Dutch Research Council (NWO), Project 864.14.005. Gil Averbuch is funded through the Marie Curie Action WAVES from the European Union within H2020, Grant Number 641943.

Appendix A. Supplementary material

Supplementary material related to this article can be found online at https://doi.org/10.1016/j.epsl.2021.116795.

References

Arrowsmith, S.J., Johnson, J.B., Drob, D.P., Hedlin, M.A.H., 2010. The seismoacoustic wavefield: a new paradigm in studying geophysical phenomena. Rev. Geophys. 48, 23. https://doi.org/10.1029/2010RG000335.

Assink, J.D., Averbuch, G., Shani-Kadmiel, S., Smets, P.S.M., Evers, L.G., 2018. A seismo-acoustic analysis of the 2017 North Korean nuclear test. Seismol. Res. Lett. 86, 2025–2033. https://doi.org/10.1785/0220180137.

Assink, J., Smets, P., Marcillo, O., Weemstra, C., Lalande, J.-M., Waxler, R., Evers, L., 2019. Advances in infrasonic remote sensing methods. In: Le Pichon, A., Blanc, E., Hauchecorne, A. (Eds.), Infrasound Monitoring for Atmospheric Studies. Springer International Publishing, Cham, pp. 605–632.

Averbuch, G., Assink, J.D., Evers, L.G., 2020a. Long-range atmospheric infrasound propagation from subsurface sources. J. Acoust. Soc. Am. 147, 1264–1274. https://doi.org/10.1121/10.0000792.

Averbuch, G., Waxler, R.M., Smets, P.S.M., Evers, L.G., 2020b. Probabilistic inversion for submerged source depth and strength from infrasound observations. J. Acoust. Soc. Am. 147, 1066–1077. https://doi.org/10.1121/10.0000695.

Bilham, R., 2010. Invisible faults under shaky ground. Nat. Geosci. 3, 743–745. https://doi.org/10.1038/ngeo1000.

Blanc, E., Ceranna, L., Hauchecorne, A., Charlton-Perez, A., Marchetti, E., Evers, L.G., Kvaerna, T., Lastovicka, J., Eliasson, L., Crosby, N.B., Blanc-Benon, P., Le Pichon, A., Brachet, N., Pilger, C., Keckhut, P., Assink, J.D., Smets, P.S.M., Lee, C.F., Kero, J., Sindelarova, T., Kämpfer, N., Rüfenacht, R., Farges, T., Millet, C., Näsholm, S.P., Gibbons, S.J., Espy, P.J., Hibbins, R.E., Heinrich, P., Ripepe, M., Khaykin, S., Mze, N., Chum, J., 2017. Toward an improved representation of middle atmospheric dynamics thanks to the ARISE project. Surv. Geophys., D2S04. https://doi.org/10.1007/s10712-017-9444-0.

Bolt, B.A., 1964. Seismic air waves from the great 1964 Alaskan earthquake. Nature 202, 1095–1096. https://doi.org/10.1038/2021095a0.

Corbane, C., Saito, K., Dell'Oro, L., Bjorgo, E., Gill, S.P., Emmanuel Piard, B., Huyck, C.K., Kemper, T., Lemoine, G., Spence, R.J., Shankar, R., Senegas, O., Ghesquiere, F., Lallemant, D., Evans, G.B., Gartley, R.A., Toro, J., Ghosh, S., Svekla, W.D., Adams, B.J., Eguchi, R.T., 2011. A comprehensive analysis of building damage in the 12 January 2010 Mw7 Haiti earthquake using high-resolution satellite and aerial imagery. Photogramm. Eng. Remote Sens. 77, 997–1009. https://doi.org/10.14358/PERS.77.10.0997.

Dahlman, O., Mykkeltveit, S., Haak, H., 2009. Nuclear Test Ban: Converting Political Visions to Reality.

Douilly, R., Haase, J.S., Ellsworth, W.L., Bouin, M.-P., Calais, E., Symithe, S.J., Armbruster, J.G., de Lepinay, B.M., Deschamps, A., Mildor, S.-L., Meremonte, M.E., Hough, S.E., 2013. Crustal structure and fault geometry of the 2010 Haiti earthquake from temporary seismometer deployments. Bull. Seismol. Soc. Am. 103, 2305–2325. https://doi.org/10.1785/0120120303.

Drob, D.P., Emmert, J.T., Meriwether, J.W., Makela, J.J., Doornbos, E., Conde, M., Hernandez, G., Noto, J., Zawdie, K.A., McDonald, S.E., Huba, J.D., Klenzing, J.H., 2015. An update to the horizontal wind model (HWM): the quiet time thermosphere: empirical model of thermospheric winds. Earth Space Sci. 2, 301–319. https://doi.org/10.1002/2014EA000089.

Earle, P.S., Wald, D.J., Jaiswal, K.S., Allen, T.I., Hearne, M.G., Marano, K.D., Hotovec, A.J., Fee, J., 2009. Prompt assessment of global earthquakes for response (PAGER): a system for rapidly determining the impact of earthquakes worldwide.

Evers, L.G., Brown, D., Heaney, K.D., Assink, J.D., Smets, P.S.M., Snellen, M., 2014. Evanescent wave coupling in a geophysical system: airborne acoustic signals from the Mw 8.1 Macquarie Ridge earthquake. Geophys. Res. Lett. https://doi.org/10.1002/2013GL058801.

Evers, L.G., Haak, H.W., 2007. Infrasonic forerunners: exceptionally fast acoustic phases. Geophys. Res. Lett. 34, 1–5. https://doi.org/10.1029/2007GL029353.

Francis, G., Stuart, G., Galen, E., Ross, G., Joaquin, B.A., Toro, Paul A., John, B., Lawrence, C., Ron, E., Michael, E., Shubharoop, G., Matt, H., Zenghui, H., Charles, H., Melisa, H., Walter, S., Enrica, V., Su, W., 2016. Post-disaster building damage assessment using satellite and aerial imagery interpretation, field verification and modeling techniques. 2010 Haiti earthquake - Final report. A World Bank, GFDRR and ImageCat report. http://learningfromearthquakes.org/2010-01-12-haiti/11-resources/121-post-disaster-building-damage-assessment-using-satellite-and-aerial-imagery-interpretation-field-verification-and-modeling-techniques. (Accessed October 2020).

Frankel, A., Harmsen, S., Mueller, C., Calais, E., Haase, J., 2010. Documentation for initial seismic hazard maps for Haiti.

Gabrielson, T., 2011. In situ calibration of atmospheric-infrasound sensors including the effects of wind-noise-reduction pipe systems. J. Acoust. Soc. Am. 130, 1154–1163. https://doi.org/10.1121/1.3613925.

Garcia, R.F., Bruinsma, S., Lognonné, P., Doornbos, E., Cachoux, F., 2013. GOCE: the first seismometer in orbit around the Earth. Geophys. Res. Lett. 40, 1015–1020. https://doi.org/10.1002/grl.50205.

Godin, O.A., 2002. An effective quiescent medium for sound propagating through an inhomogeneous, moving fluid. J. Acoust. Soc. Am. 112, 1269–1275. https://doi.org/10.1121/1.1504853.

Godin, O.A., 2008. Sound transmission through water–air interfaces: new insights into an old problem. Contemp. Phys. 49, 105–123. https://doi.org/10.1080/00107510802090415.

Godin, O.A., 2011. Low-frequency sound transmission through a gas–solid interface. J. Acoust. Soc. Am. 129, EL45–EL51. https://doi.org/10.1121/1.3535578.

Green, D.N., Guilbert, J., Le Pichon, A., Sebe, O., Bowers, D., 2009. Modelling ground-to-air coupling for the shallow ML 4.3 Folkestone, United Kingdom, earthquake of 28 April 2007. Bull. Seismol. Soc. Am. 99, 2541–2551. https://doi.org/10.1785/0120080236.

Hayes, G.P., Briggs, R.W., Sladen, A., Fielding, E.J., Prentice, C., Hudnut, K., Mann, P., Taylor, F.W., Crone, A.J., Gold, R., Ito, T., Simons, M., 2010. Complex rupture during the 12 January 2010 Haiti earthquake. Nat. Geosci. 3, 800–805. https://doi.org/10.1038/ngeo977.

Hedlin, M.A.H., Raspet, R., 2003. Infrasonic wind-noise reduction by barriers and spatial filters. J. Acoust. Soc. Am.

Hernandez, B., Le Pichon, A., Vergoz, J., Herry, P., Ceranna, L., Pilger, C., Marchetti, E., Ripepe, M., Bossu, R., 2018. Estimating the ground-motion distribution of the 2016 Mw 6.2 Amatrice, Italy, earthquake using remote infrasound observations. Seismol. Res. Lett. https://doi.org/10.1785/0220180103.

Hough, S.E., Altidor, J.R., Anglade, D., Given, D., Janvier, M.G., Maharrey, J.Z., Meremonte, M., Mildor, B.S.-L., Prepetit, C., Yong, A., 2010. Localized damage caused by topographic amplification during the 2010 M 7.0 Haiti earthquake. Nat. Geosci. 3, 778–782. https://doi.org/10.1038/ngeo988.

Hough, S.E., Taniguchi, T., Altidor, J.-R., 2012. Estimation of peak ground acceleration from horizontal rigid body displacement: a case study in Port-au-Prince, Haiti. Bull. Seismol. Soc. Am. 102, 2704–2713. https://doi.org/10.1785/0120120047.

Hunter, J.D., 2007. Matplotlib: a 2D graphics environment. Comput. Sci. Eng. 9, 90–95. https://doi.org/10.1109/MCSE.2007.55.

Jaiswal, K., Wald, D., Earle, P., Porter, K., Hearne, M., 2011. Earthquake casualty models within the USGS prompt assessment of global earthquakes for response (PAGER) system. In: Spence, R., So, E., Scawthorn, C. (Eds.), Human Casualties in Earthquakes. In: Advances in Natural and Technological Hazards Research, vol. 29. Springer, Dordrecht, pp. 83–94.

Le Pichon, A., Mialle, P., Guilbert, J., Vergoz, J., 2006. Multistation infrasonic observations of the Chilean earthquake of 2005 June 13. Geophys. J. Int. 167, 838–844. https://doi.org/10.1111/j.1365-246X.2006.03190.x.

Lonzaga, J.B., Waxler, R.M., Assink, J.D., Talmadge, C.L., 2015. Modelling waveforms of infrasound arrivals from impulsive sources using weakly non-linear ray theory. Geophys. J. Int. 200, 1347–1361. https://doi.org/10.1093/gji/ggu479.

Marchetti, E., Lacanna, G., Le Pichon, A., Piccinini, D., Ripepe, M., 2016. Evidence of large infrasonic radiation induced by earthquake interaction with alluvial sediments. Seismol. Res. Lett. 87, 678–684. https://doi.org/10.1785/0220150223.

Melton, B.S., Bailey, L.F., 1957. Multiple signal correlators. Geophysics 22, 565–588.

Mercier de Lépinay, B., Deschamps, A., Klingelhoefer, F., Mazabraud, Y., Delouis, B., Clouard, V., Hello, Y., Crozon, J., Marcaillou, B., Graindorge, D., Vallée, M., Perrot, J., Bouin, M.-P., Saurel, J.-M., Charvis, P., St-Louis, M., 2011. The 2010 Haiti earthquake: a complex fault pattern constrained by seismologic and tectonic observations. Geophys. Res. Lett. 38. https://doi.org/10.1029/2011GL049799.

Mutschlecner, J.P., Whitaker, R.W., 2005. Infrasound from earthquakes. J. Geophys. Res., Atmos. 110. https://doi.org/10.1029/2004JD005067.

Nettles, M., Hjörleifsdóttir, V., 2010. Earthquake source parameters for the 2010 January Haiti main shock and aftershock sequence: Haiti earthquake source parameters. Geophys. J. Int. 183, 375–380. https://doi.org/10.1111/j.1365-246X.2010.04732.x.

Nippress, A., Green, D., 2019. Global empirical models for infrasonic signal celerity, backazimuth and duration from ground truth data. In: AGU Fall Meeting. San Francisco, California, 6 - 13 December.

Picone, J.M., Hedin, A.E., Drob, D.P., Aikin, A.C., 2002. NRLMSISE-00 empirical model of the atmosphere: statistical comparisons and scientific issues: TECHNIQUES. J. Geophys. Res. 107, SIA 15-1. https://doi.org/10.1029/2002JA009430.

Pilger, C., Ceranna, L., Ross, J.O., Vergoz, J., Le Pichon, A., Brachet, N., Blanc, E., Kero, J., Liszka, L., Gibbons, S., Kvaerna, T., Näsholm, S.P., Marchetti, E., Ripepe, M., Smets, P., Evers, L., Ghica, D., Ionescu, C., Sindelarova, T., Ben Horin, Y., Mialle, P., 2018. The European infrasound bulletin. Pure Appl. Geophys. 175, 3619–3638. https://doi.org/10.1007/s00024-018-1900-3.

Possee, D., Keir, D., Harmon, N., Rychert, C., Rolandone, F., Leroy, S., Corbeau, J., Stuart, G., Calais, E., Illsley-Kemp, F., Boisson, D., Momplaisir, R., Prépetit, C., 2019. The tectonics and active faulting of Haiti from seismicity and tomography. Tectonics 38, 1138–1155. https://doi.org/10.1029/2018TC005364.

Shani-Kadmiel, S., Assink, J.D., Smets, P.S.M., Evers, L.G., 2018. Seismoacoustic coupled signals from earthquakes in Central Italy: epicentral and secondary sources of infrasound. Geophys. Res. Lett. 45, 427–435. https://doi.org/10.1002/2017GL076125.

Smets, P., 2018. Infrasound and the dynamical stratosphere: a new application for operational weather and climate prediction. https://doi.org/10.4233/uuid:517f8597-9c24-4d01-83ed-0f430353e905.

Sutherland, L.C., Bass, H.E., 2004. Atmospheric absorption in the atmosphere up to 160 km. J. Acoust. Soc. Am. 115, 1012–1032. https://doi.org/10.1121/1.1631937.

Walker, K.T., Le Pichon, A., Kim, T.S., de Groot-Hedlin, C., Che, I.Y., Garcés, M., 2013. An analysis of ground shaking and transmission loss from infrasound generated by the 2011 Tohoku earthquake. J. Geophys. Res., Atmos. 118, 831–851. https://doi.org/10.1002/2013JD020187.

Wapenaar, C., Berkhout, A. (Eds.), 1989. Elastic Wave Field Extrapolation, vol. 2. Elsevier.

Waxler, R., Assink, J., 2019. Propagation modeling through realistic atmosphere and benchmarking. In: Le Pichon, A., Blanc, E., Hauchecorne, A. (Eds.), Infrasound Monitoring for Atmospheric Studies. Springer International Publishing, Cham, pp. 509–549.

Wessel, P., Luis, J.F., Uieda, L., Scharroo, R., Wobbe, F., Smith, W.H.F., Tian, D., 2019. The generic mapping tools version 6. Geochem. Geophys. Geosyst. 20, 5556–5564. https://doi.org/10.1029/2019GC008515.